

Supplementary Information

Boosting Pt atom efficiency by reinforcing the synergy with extra Sn sites encapsulated in MFI zeolite for the aromatization of n-hexane

LinKun Yan^{1,2}, Guodong Liu¹, Xin Shang^{*1}, Xiong Su^{*1}, Yanqiang Huang¹

¹State Key Laboratory of Catalysis, Dalian Institute of Chemical Physics, Chinese Academy of Sciences, No. 457 Zhongshan Road, Dalian 116023, China.

²University of Chinese Academy of Sciences, Beijing 100049, China.

* Corresponding authors, E-mail: shangxin@dicp.ac.cn, suxiong@dicp.ac.cn.

Table S1. Chemical composition and the dispersion of Pt in $\text{Pt}_x\text{Sn}_y@\text{S}-1$ samples.

Samples	Metal loading ^a			Dispersion of Pt atoms ^b
	K	Pt	Sn	
$\text{Sn}_1@\text{S}-1$	0.58	/	1.32	/
$\text{Pt}_{0.1}@\text{S}-1$	0.41	0.12	/	29.0
$\text{Pt}_{0.1}\text{Sn}_{0.5}@\text{S}-1$	0.45	0.13	0.65	48.8
$\text{Pt}_{0.1}\text{Sn}_1@\text{S}-1$	0.45	0.11	1.07	44.4
$\text{Pt}_{0.1}\text{Sn}_2@\text{S}-1$	0.73	0.11	2.76	47.9

a: wt%, provided by ICP-OES analysis.

b: %, provided by CO-pulse tests assuming that CO is singly absorbed on Pt atoms.

Table S2. Textural properties of the $\text{Pt}_x\text{Sn}_y@\text{S}-1$ samples determined by N_2 -physical adsorption-desorption characterizations.

Samples	S_{BET}	S_{Micro}	S_{Exsurf}	V_{Micro}
$\text{Pt}_{0.1}@\text{S}-1$	449	185	264	0.10
$\text{Pt}_{0.1}\text{Sn}_{0.5}@\text{S}-1$	435	197	238	0.09
$\text{Pt}_{0.1}\text{Sn}_1@\text{S}-1$	431	195	236	0.11
$\text{Pt}_{0.1}\text{Sn}_2@\text{S}-1$	445	201	244	0.11

S: $\text{m}^2 \text{ g}^{-1}$

V: $\text{cm}^3 \text{ g}^{-1}$

Table S3. Fitting results of Mössbauer spectroscopy for Sn₁@S-1 and Pt_{0.1}Sn₁@S-1.

	Doublet (1)	Doublet (2)
Sn₁@S-1		
IS	-0.15	2.74
QS	2.74	1.95
Percentage	23.34	76.66
Pt_{0.1}Sn₁@S-1		
IS	0	2.72
QS	0.56	1.95
Percentage	10.10	89.90

IS: mm s⁻¹, QS: mm s⁻¹, Percentage: %

Mössbauer spectroscopy features a large quadrupole splitting parameter ($\Delta > 1.9 \text{ mm s}^{-1}$), suggesting that Sn exhibits a stereo-active lone pair.¹ Moreover, the spectrum reveals that the isomer shift (IS) of Sn₁@S-1 (-0.15 mm s⁻¹) is lower than that of Sn(IV) (-0.03 mm s⁻¹), implying the decreased electron density of Sn atoms as a result of the varied coordination environment within the zeolite framework.²

Table S4. Fitting results for the Sn edge of EXAFS spectra of $\text{Sn}_1@\text{S-1}$ and $\text{Pt}_{0.1}\text{Sn}_1@\text{S-1}$.

sample	$N_{\text{Sn-O}}$	$R_{\text{Sn-O}} (\text{\AA})$	$\sigma^2 (\text{\AA}^2)$	$\Delta E_0 (\text{eV})$	R-factor
SnO	4	2.213 ± 0.010	0.0092 ± 0.0015	2.2 ± 1.0	0.0111
SnO_2	6	2.042 ± 0.009	0.0021 ± 0.0007	0.9 ± 0.9	0.0045
$\text{Sn}_1@\text{S-1}$	4.2 ± 0.4	2.036 ± 0.009	0.0049 ± 0.0013	0.2 ± 1.3	0.0107
$\text{Pt}_{0.1}\text{Sn}_1@\text{S-1}$	3.8 ± 0.4	2.047 ± 0.010	0.0052 ± 0.0014	1.2 ± 1.2	0.0123

R, bonding distance; σ^2 , Debye-Waller factor; ΔE_0 , inner potential correction; R_factor, difference between modelled and experimental data. For $\text{Sn}@\text{S-1}$ and $\text{PtSn}@{\text{S-1}}$, the fits of the Sn edge were performed on the first coordination shell ($\Delta R = 1.0\text{-}3.0\text{\AA}$) over Fourier transform (FT) of the $k^1 k^2 k^3$ -weighted $\chi(k)$ functions in the range $\Delta k = 3.0\text{-}10.5\text{\AA}^{-1}$, where Δk and ΔR are the intervals in the k and R spaces for the Fourier transformation and the fit, respectively, resulting in several independent parameters of $2\Delta R \Delta k/\pi = 9.5$. The many-body amplitude reduction factor amp = 1.13.

Table S5. Acidity properties of $\text{Pt}_x\text{Sn}_y@\text{S}-1$ samples.

Samples	Acid content ^a	Lewis acid ^b	H-bonded pyridine
$\text{Sn}_1@\text{S}-1$	5.2	20.2	32.6
$\text{Pt}_{0.1}@\text{S}-1$	1.4	0.7	0.7
$\text{Pt}_{0.1}\text{Sn}_{0.5}@\text{S}-1$	4.4	14.5	27.9
$\text{Pt}_{0.1}\text{Sn}_1@\text{S}-1$	5.0	18.1	36.9
$\text{Pt}_{0.1}\text{Sn}_2@\text{S}-1$	6.3	30.6	24.7

a: $\text{mL}_{\text{NH}_3} \text{g}^{-1}$, tested by $\text{NH}_3\text{-TPD}$.

b: $\mu\text{mol g}^{-1}$, tested by Py-IR, based on the integrated IR peak areas at the 1452 cm^{-1} band.

c: $\mu\text{mol g}^{-1}$, tested by Py-IR, based on the integrated IR peak areas at the 1444 cm^{-1} band.

Table S6. The attribution of absorbance peaks in *in situ* infrared (TPD-DRIFTS) test.

Wavenumber (cm^{-1})	Attribution
1-hexene	
3080	asymmetric $=\text{CH}_2$ stretching vibration
2997	symmetric $=\text{CH}_2$ stretching vibration
2960	asymmetric $-\text{CH}_3$ stretching vibration
2924	asymmetric $-\text{CH}_2$ stretching vibration
2870	symmetric $-\text{CH}_3$ stretching vibration
2861	asymmetric $-\text{CH}_2$ stretching vibration
cyclohexene	
3067, 3026	The C–H stretch of the C=C–H
2938, 2862, 2841	–C–H stretching

The absorption peak position showed a shift or change due to differences in test methods and the fact that 1-hexene and cyclohexene are adsorbed on the zeolite in this experiment.³

Table S7. Performance detail of the comparative catalysts in Figure 2e.

	Temperature	Carrier gas	Reactant	Carrier gas/ Reactant (mol/mol)	WHSV (h ⁻¹)	Yield (%)	Pt loading (wt%)	Specific activity (g g _{Pt} ⁻¹ h ⁻¹)
This work	550	Ar	<i>n</i> -hexane	7	2	62.4	0.12	856.5
10Pt/KL ⁴	420	H ₂	<i>n</i> -heptane	6	0.68	58.1	0.19	205.3
Pt/Beta-Rb ⁵	550	H ₂	<i>n</i> -heptane	6	2	76.6	0.7	152.6
PtFe-1/KL ⁶	420	H ₂	<i>n</i> -octane	6	0.68	89.1	0.21	230.4
Pt/KL(Sn) ⁷	500	H ₂	<i>n</i> -octane	6	0.7	67.1	0.15	386.4
PtZn/KL ⁸	500	H ₂	<i>n</i> -heptane	6	0.68	62.5	0.4	104.9
Pt/KL-2 ⁹	450	H ₂	<i>n</i> -hexane	6	1	59.6	0.12	472.1
Pt/KYC2 ¹⁰	500	H ₂	<i>n</i> -octane	6	0.7	/	0.13	298.1
Pt/CeO ₂ ¹¹	400	H ₂	<i>n</i> -hexane	/	/	57.8	1.5	61.4
Pt/KL-10 ¹²	500	H ₂	<i>n</i> -heptane	6	0.68	66.3	0.21	172.1
1%Pt/KL ¹³	500	H ₂	<i>n</i> -hexane	6	2	85.7	1	120.2
Pt ₄ @KL ¹⁴	440	H ₂	<i>n</i> -hexane	6	1	68	0.33	235.4
Pt/KL ¹⁵	500	H ₂	<i>n</i> -heptane	6	1	49	0.6	104.2
Pt/Kβ ¹⁶	550	H ₂	<i>n</i> -heptane	6	2	85.2	0.25	360.5
Pt/HR-KL-1 ¹⁷	500	H ₂	<i>n</i> -hexane	6	4	55.1	1	308.9
Pt/Ba/KL ¹⁸	500	H ₂	<i>n</i> -octane	6.75	1	63.6	0.5	102.4
Pt/K-Beta ¹⁹	550	H ₂	<i>n</i> -heptane	6	2	85.3	1	117.0
Pt/BaKL ²⁰	420	H ₂	<i>n</i> -heptane	6	0.8(LHSV)	78	0.43	145.9
Pt@Sil-1-4Na ²¹	500	H ₂	<i>n</i> -hexane	2	2.7	78	0.6	318.2
Pt/CeY ²²	490	H ₂	Naphtha	9	2(LHSV)	56.1	0.3	381.3
Pt _{0.3} /Al ₂ O ₃ -Cl ²²	490	H ₂	Naphtha	9	2(LHSV)	65.4	0.3	374.0
Pt/FeKL ²³	450	H ₂	<i>n</i> -hexane	3	3	77.4	0.5	355.5
Pt@SnKL ²⁴	480	H ₂	<i>n</i> -heptane	6	0.68	62.4	0.49	98.8

The reaction pressure of all catalysts mentioned is 1atm, except 0.7 MPa for Pt/CeY and Pt_{0.3}/Al₂O₃-Cl.

The specific activity of catalysts is determined by calculating the total aromatic yield (summation of individual aromatic compound yields) in systems containing multiple aromatic species, and the M_{aromatic}/M_{alkane} is using 0.9196 (M_{toluene}/M_{*n*-heptane}), to obtain a relatively adequate value.

$$\text{Specific activity} = \frac{WHSV \times \text{Yield} \times \frac{M_{\text{aromatic}}}{M_{\text{alkane}}}}{\text{Pt loading}}$$

WHSV: h⁻¹, M: g mol⁻¹, Pt loading: wt%, Specific activity: g_{aromatic} g_{Pt}⁻¹ h⁻¹

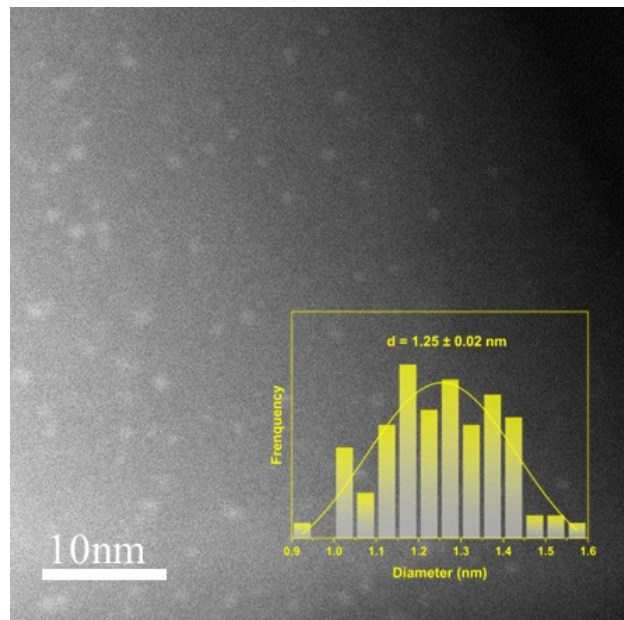


Figure S1. TEM image of $\text{Pt}_{0.1}\text{Sn}_{0.5}@\text{S}-1$

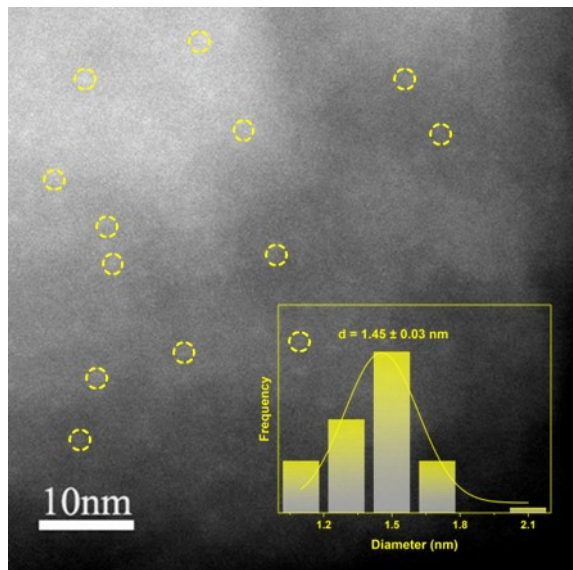


Figure S2. TEM image of $\text{Pt}_{0.1}\text{Sn}_2@\text{S}-1$

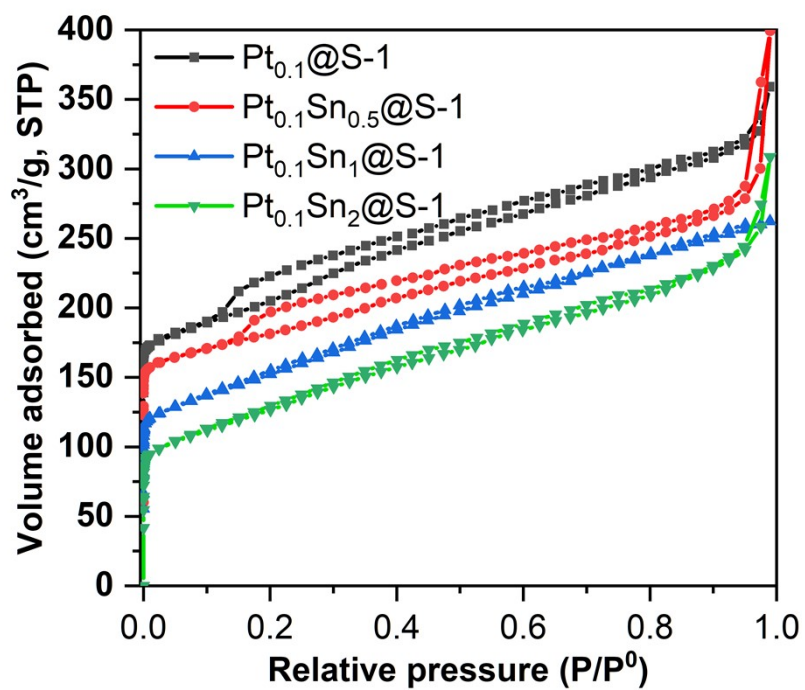


Figure S3. N_2 physical adsorption-desorption isotherms.

Curves of $\text{Pt}_{0.1}@\text{S-1}$ (black), $\text{Pt}_{0.1}\text{Sn}_{0.5}@\text{S-1}$ (red) and $\text{Pt}_{0.1}\text{Sn}_1@\text{S-1}$ (blue) have been offset upward by 80, 60, 30, respectively for easy viewing.

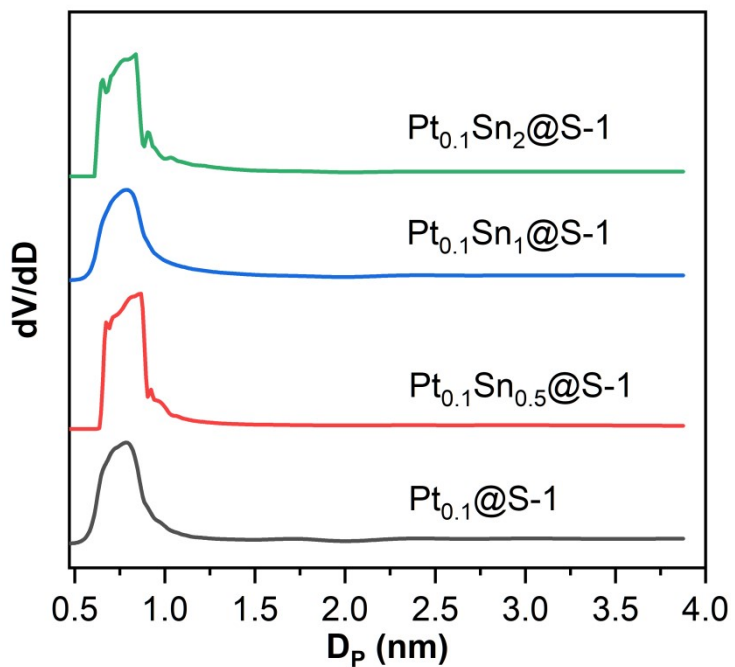


Figure S4. Pore size distribution pattern.

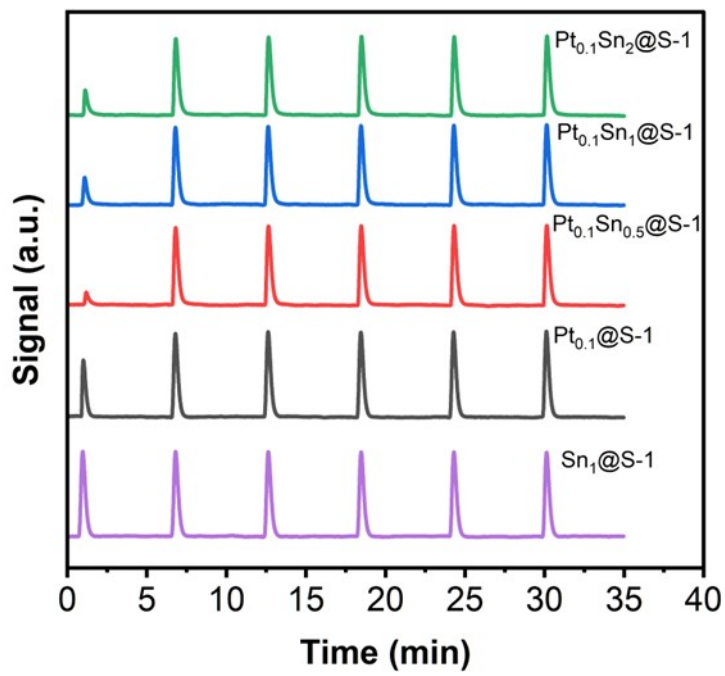


Figure S5. CO-Pulse Test.

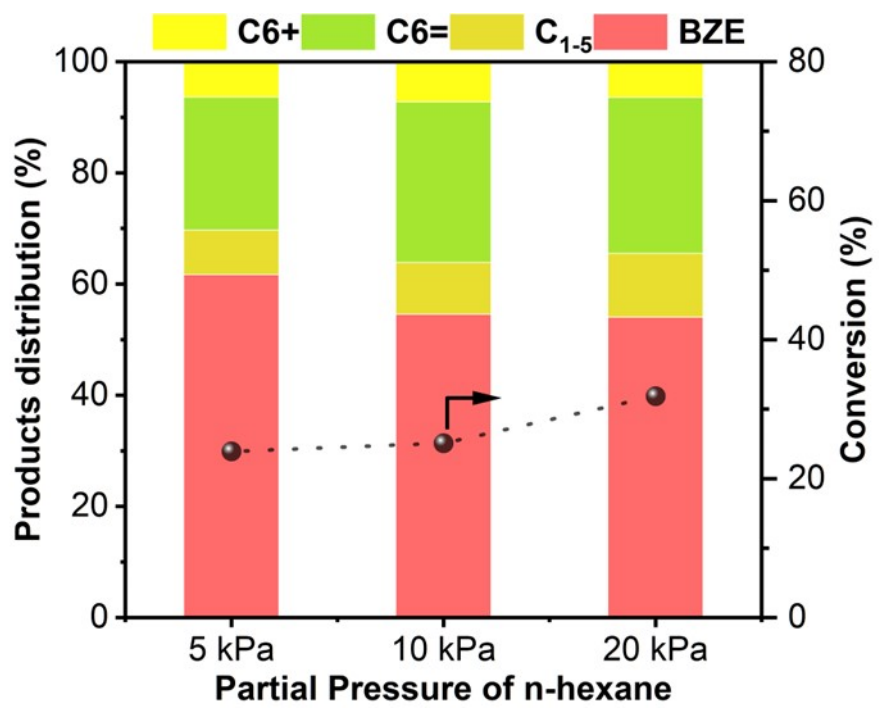


Figure S6. Catalytic performance of $\text{Pt}_{0.1}\text{Sn}_1@\text{S}-1$ at different partial pressure of n-hexane.

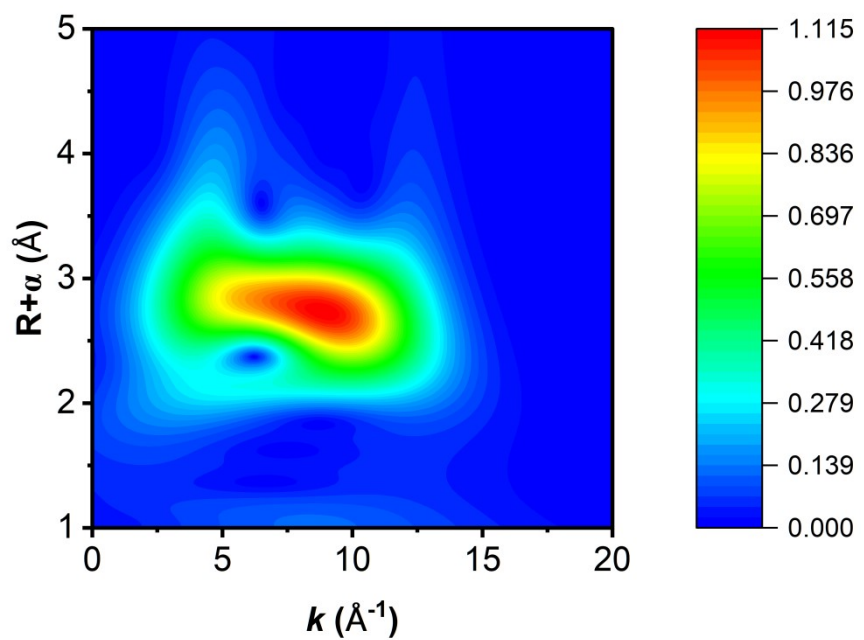


Figure S7. Wavelet transforms contour plots for the k3-weighted EXAFS signals of the Sn K-edge for Sn foil.

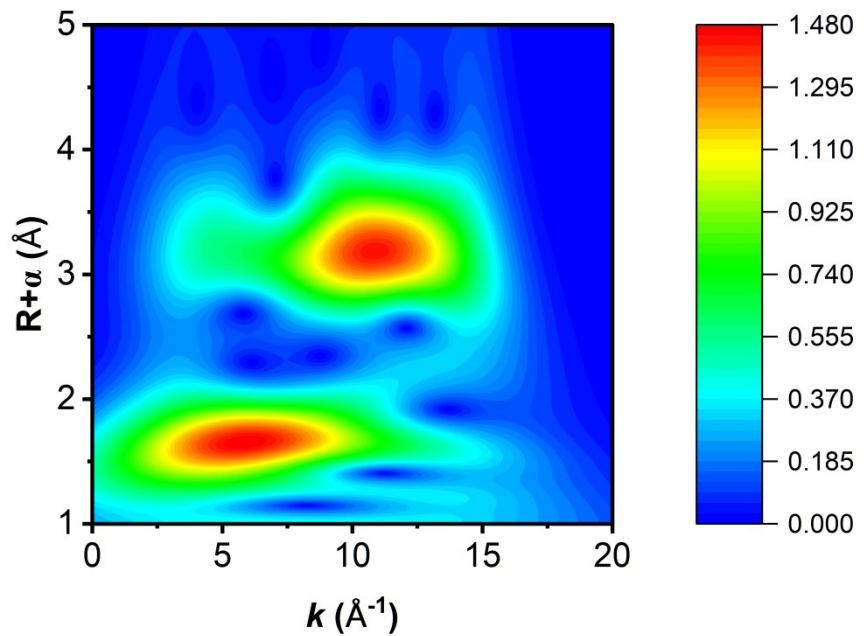


Figure S8. Wavelet transforms contour plots for the k^3 -weighted EXAFS signals of the Sn K-edge for SnO.

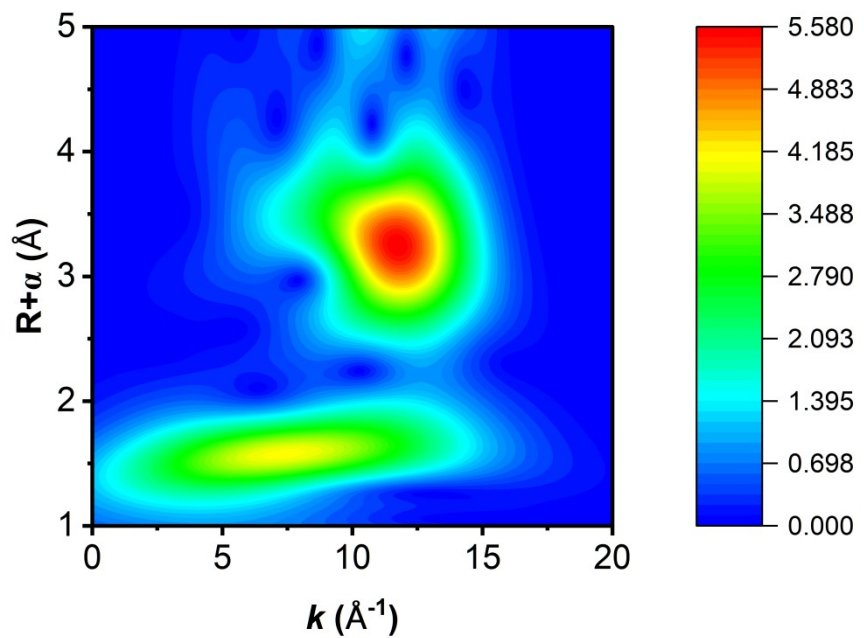


Figure S9. Wavelet transforms contour plots for the k^3 -weighted EXAFS signals of the Sn K-edge for SnO_2 .

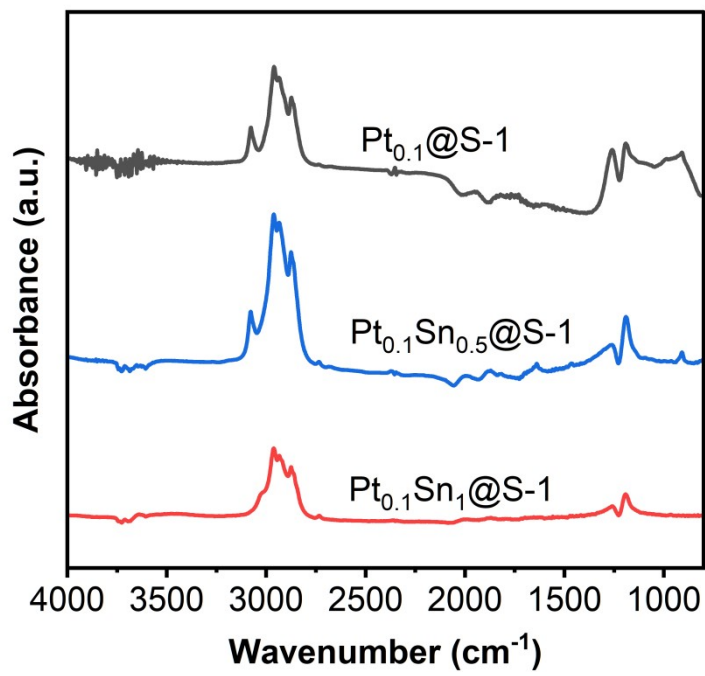


Figure S10. *in-situ* 1-hexene adsorption infrared spectra after 25 minutes of purge by Helium flow.

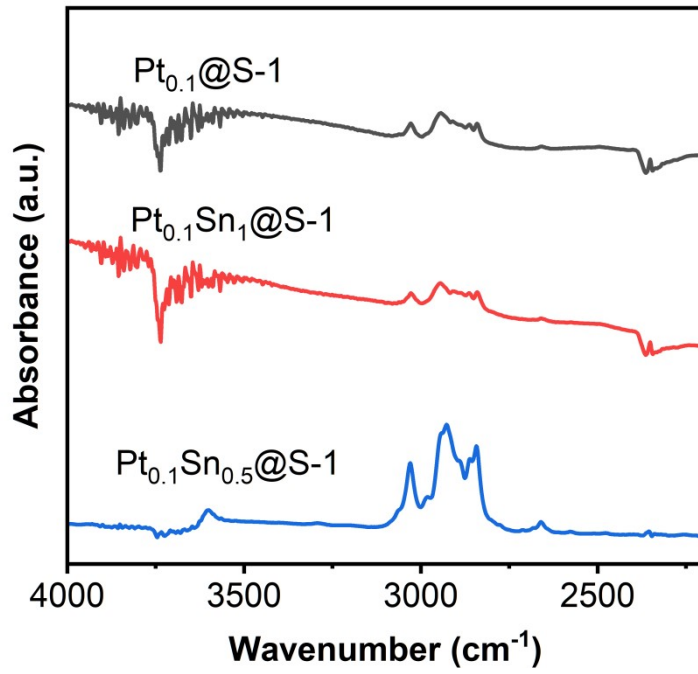


Figure S11. *in-situ* cyclohexene adsorption infrared spectra after 25 minutes of purge by Helium flow.

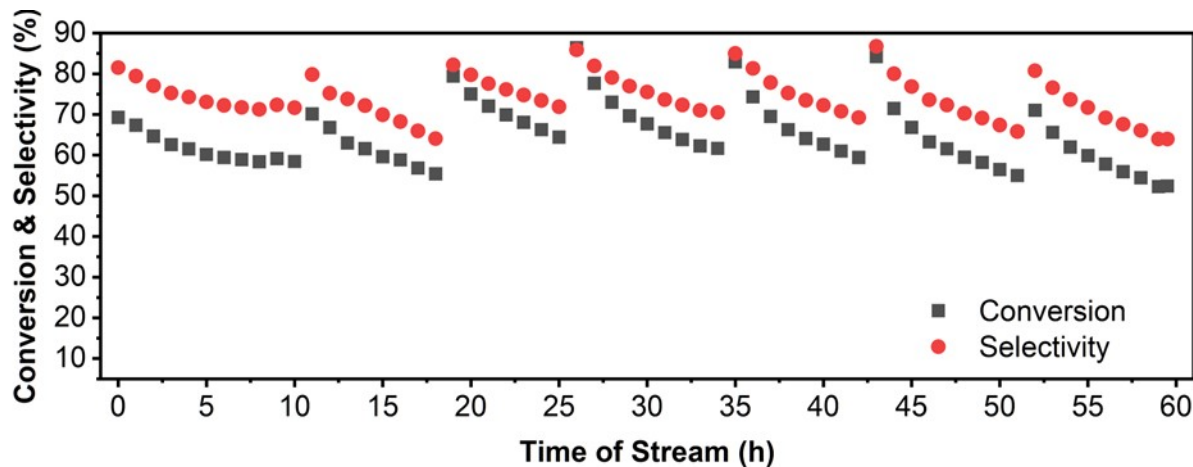


Figure S12. The regeneration test for $\text{Pt}_{0.1}\text{Sn}_1@\text{S}-1$ at $550\text{ }^\circ\text{C}$.

The regeneration experiment was conduct under a following condition: $550\text{ }^\circ\text{C}$, 0.1 MPa , $\text{WHSV} = 2\text{ h}^{-1}$, $\text{GHSV} = 3840\text{ mL g}^{-1}\text{ h}^{-1}$ ($\text{Ar : n-hexane} = 7 : 1$). After the reaction, the coke formed on the Pt-zeolite catalyst was removed by calcination in air (30 ml min^{-1}) at $550\text{ }^\circ\text{C}$ for 1.5 h . After the calcination treatment, the catalyst is reduced by H_2 flow (50% H_2/Ar gas, 30 ml min^{-1}) at $550\text{ }^\circ\text{C}$ for 1.5 h before the test.

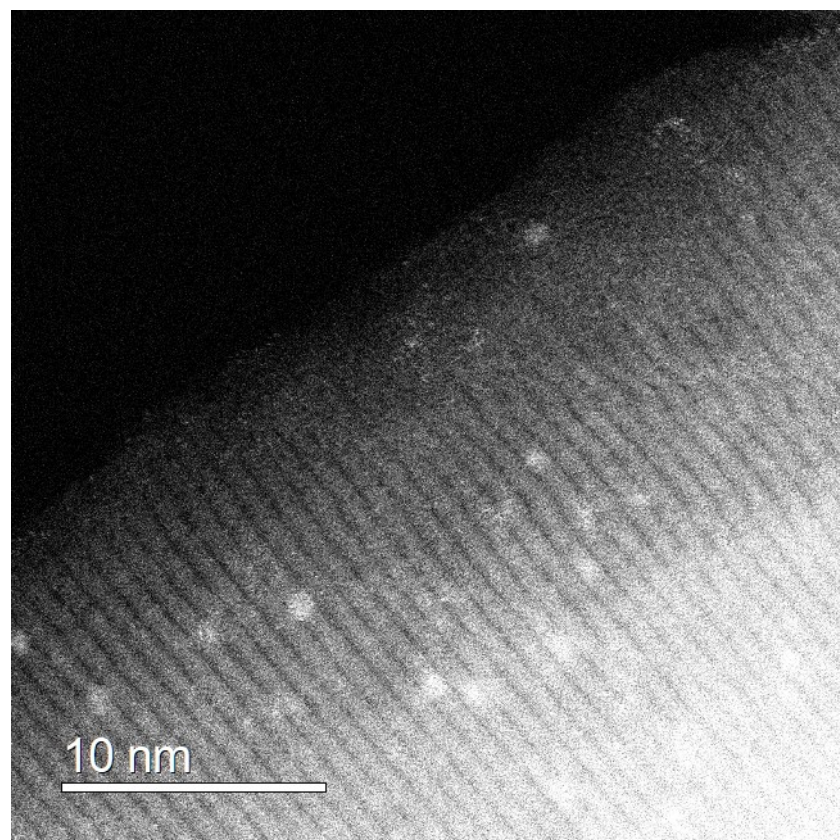


Figure S13. HAADF-STEM image of $\text{Pt}_{0.1}\text{Sn}_1@\text{S-1}$.

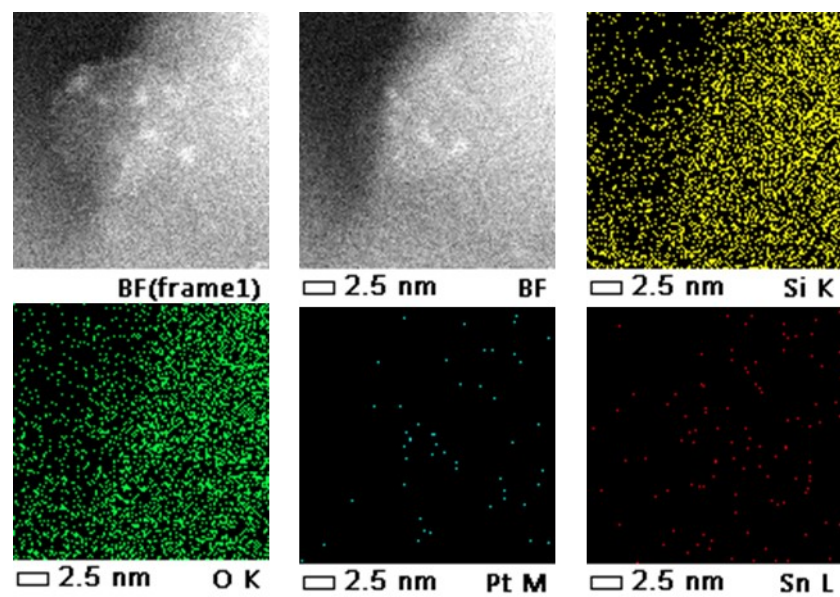


Figure S14. EDS patterns of $\text{Pt}_{0.1}\text{Sn}_1@\text{S-1}$.

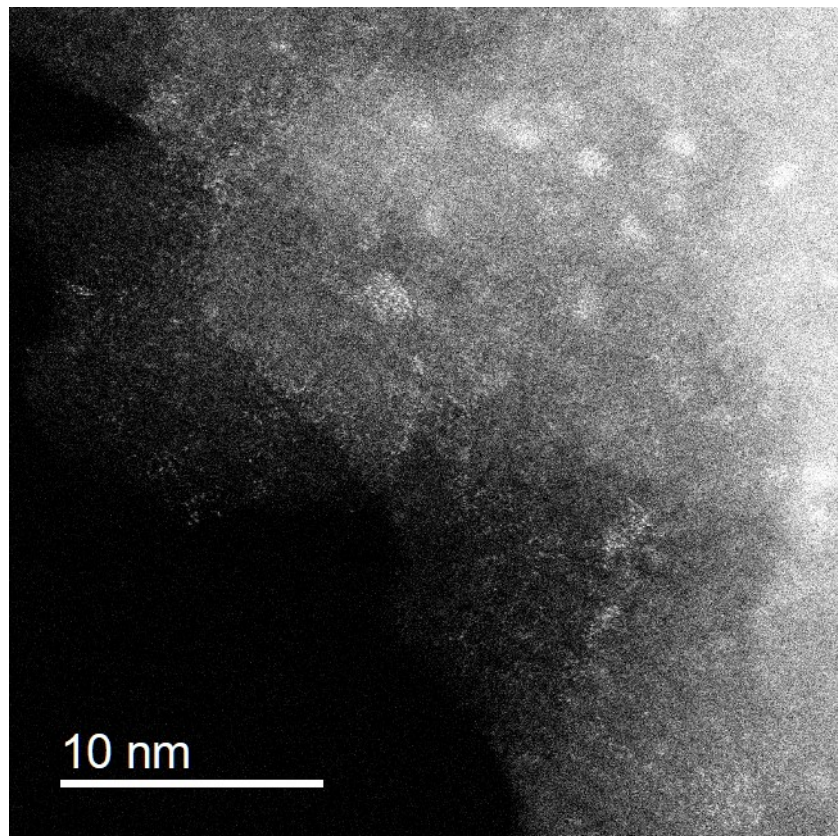


Figure S15. HAADF-STEM image of Pt_{0.1}Sn₂@S-1.

Pt particle size in Pt_{0.1}Sn₂@S-1 remains at a similar level compared to Pt_{0.1}Sn₁@S-1, and Sn species exists in a highly dispersed state. In summary, these findings demonstrate that Pt primarily exists as nanoclusters within the zeolite, while Sn is highly dispersed.

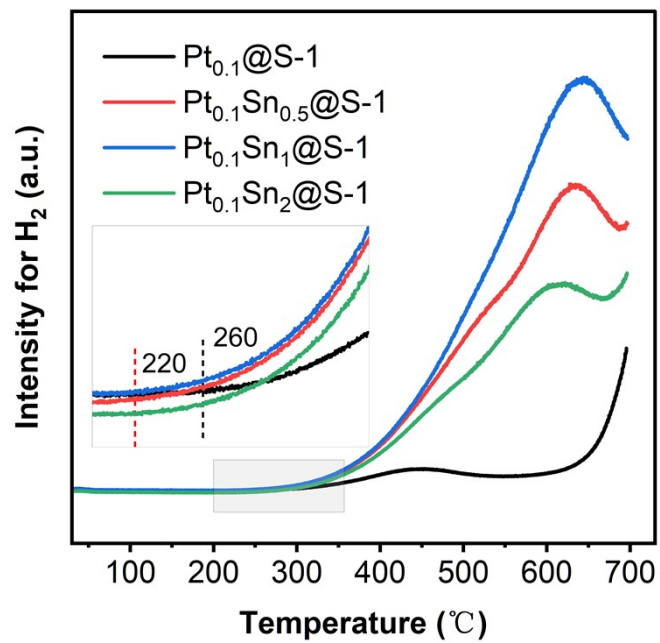


Figure S16. The signal of H₂ in TPSR test, with C₂H₆ serving as probe molecular.

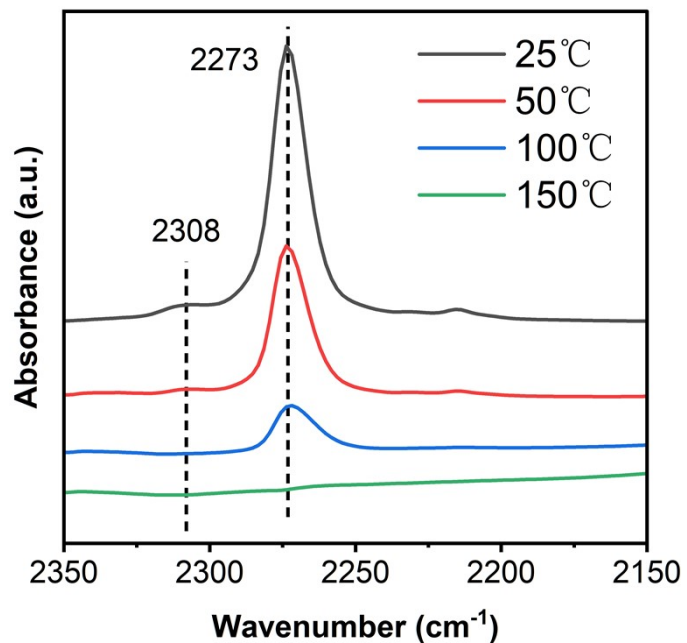


Figure S17. *In-situ* CD_3CN -IR spectra of $\text{Pt}_x\text{Sn}_y@\text{S}-1$ catalysts.

IR bands at 2273 and 2308 cm^{-1} can be assigned to CD_3CN adsorbed at silanol groups and Lewis acid sites, respectively.

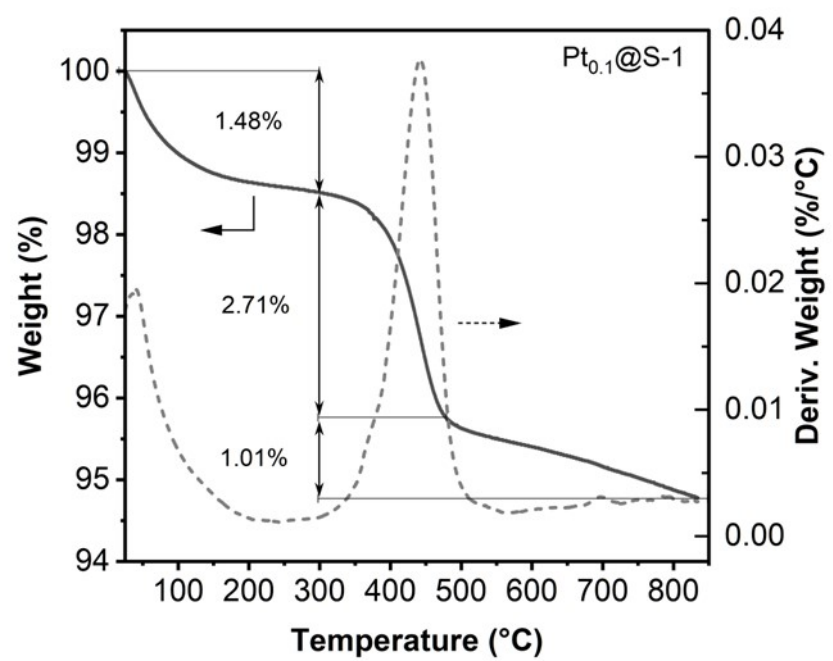


Figure S18. TGA analysis of $\text{Pt}_{0.1}@\text{S}-1$ after reaction.

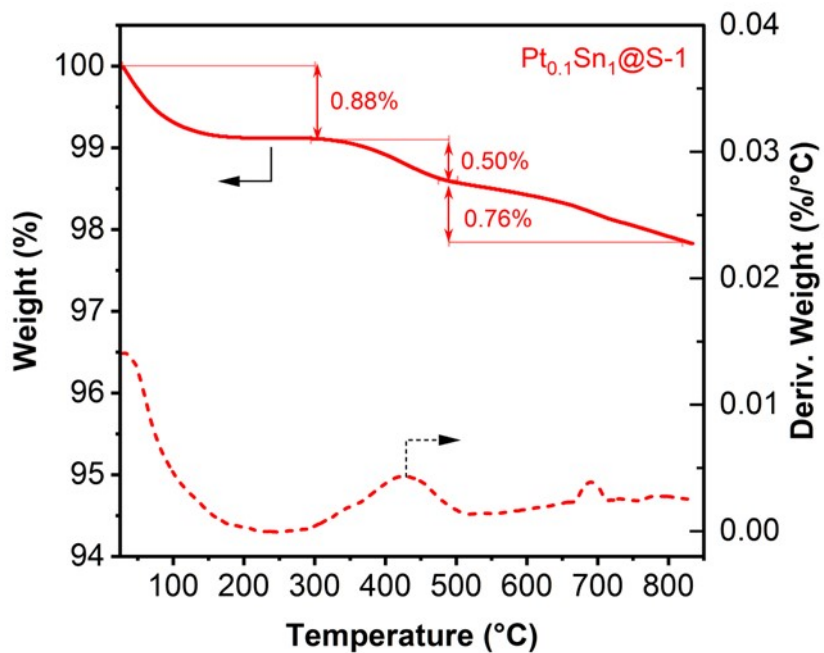


Figure S19. TGA analysis of $\text{Pt}_{0.1}\text{Sn}_1@\text{S-1}$ after reaction.

The weight losses of $\text{Pt}_{0.1}@\text{S-1}$ and $\text{Pt}_{0.1}\text{Sn}_1@\text{S-1}$ catalysts before $300\text{ }^\circ\text{C}$ were 1.48% and 0.88%, respectively, which can be attributed to adsorbed organic compounds or water impurities. The weight loss between $300\text{ }^\circ\text{C}$ and $830\text{ }^\circ\text{C}$ is ascribed to coke deposition. Notably, the coke content of $\text{Pt}_{0.1}\text{Sn}_1@\text{S-1}$ was only 1.26%, significantly lower than that of $\text{Pt}_{0.1}@\text{S-1}$ (3.72%). We further divided the coke weight loss into two stages: the weight loss between $300\text{ }^\circ\text{C}$ and $475\text{ }^\circ\text{C}$ can be attributed to soft coke, with $\text{Pt}_{0.1}@\text{S-1}$ showing a substantial weight loss of 2.71% in this stage, while $\text{Pt}_{0.1}\text{Sn}_1@\text{S-1}$ exhibited only 0.5% weight loss in the comparable temperature range of $300\text{ }^\circ\text{C}$ to $490\text{ }^\circ\text{C}$. The weight loss above $475\text{ }^\circ\text{C}$ ($490\text{ }^\circ\text{C}$) can be assigned to hard coke, possibly graphitic carbon or highly aromatic compounds, where both catalysts showed similar coke deposition. These results demonstrate that the bimetallic $\text{Pt}_x\text{Sn}_y@\text{S-1}$ primarily suppresses the formation of soft coke. Overall, the addition of Sn significantly inhibits coke accumulation during the reaction, which is crucial for maintaining catalyst stability.

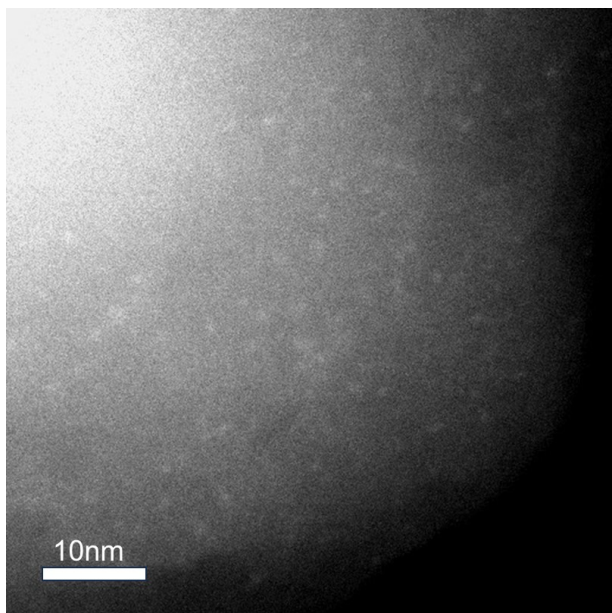


Figure S20. HRTEM image of $\text{Pt}_{0.1}\text{Sn}_1@\text{S}-1$ after reaction.

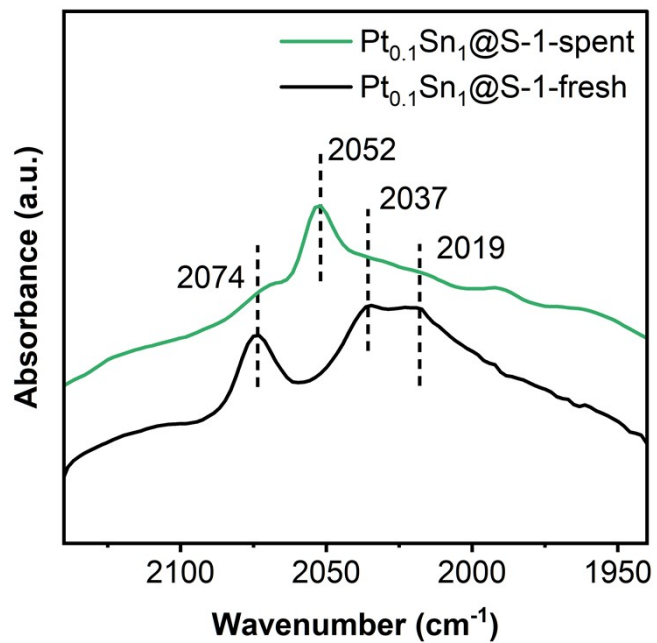


Figure S21. CO-IR spectra of $\text{Pt}_{0.1}\text{Sn}_1@\text{S-1}$ after reaction.

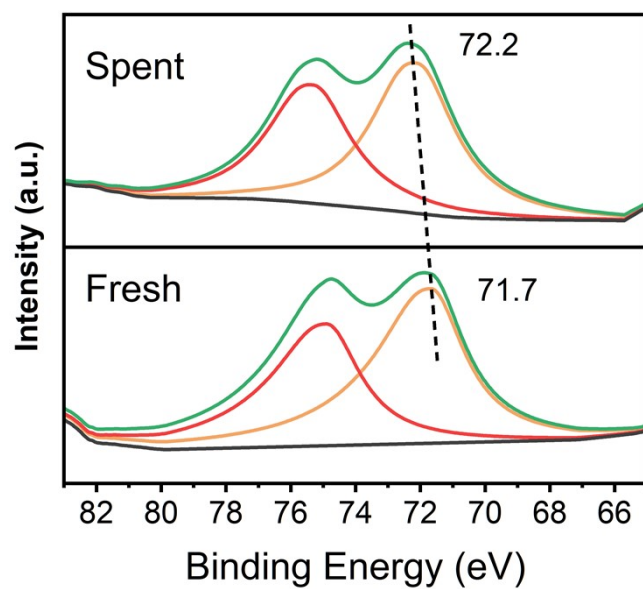


Figure S22. XPS spectra of Pt 4f for fresh and spent $\text{Pt}_{0.1}\text{Sn}_1@\text{S}-1$.

Reference

1. B. Mercadier, S. W. Coles, M. Duttine, C. Legein, M. Body, O. J. Borkiewicz, O. Lebedev, B. J. Morgan, C. Masquelier and D. Dambourret, *Journal of the American Chemical Society*, 2023, **145**, 23739-23754.
2. R. Chen, J. Zhao, Y. Li, Y. Cui, Y.-R. Lu, S.-F. Hung, S. Wang, W. Wang, G. Huo, Y. Zhao, W. Liu, J. Wang, H. Xiao, X. Li, Y. Huang and B. Liu, *Journal of the American Chemical Society*, 2023, **145**, 20683-20691.
3. W. Wu, L. M. Savereide, J. Notestein and E. Weitz, *Applied Surface Science*, 2018, **445**, 548-554.
4. D. Xu, S. Wang, B. Wu, C. Huo, Y. Qin, B. Zhang, J. Yin, L. Huang, X. Wen, Y. Yang and Y. Li, *Journal of Catalysis*, 2018, **365**, 163-173.
5. S. Ying, Z. Qiuming, Q. Zhangfeng, W. Zhiwei, J. Weiyong, D. Mei, F. Weibin and W. Jianguo, *Microporous and Mesoporous Materials*, 2022, **343**, 112189.
6. D. Xu, S. Wang, B. Wu, B. Zhang, Y. Qin, C. Huo, L. Huang, X. Wen, Y. Yang and Y. Li, *Acs Applied Materials & Interfaces*, 2019, **11**, 29858-29867.
7. Y. Mengxia, W. Baoshan, Y. Yong and L. Yongwang, *Catalysis Science & Technology*, 2023, **13**, 1677-1685.
8. D. Xu, L. Wei, M. Yan, F. Yi, G. Zhao, A. Jia, D. Zhu, S. Wang and Y. Li, *Applied Catalysis A: General*, 2023, **663**, 119308.
9. M. Yan, D. Xu, B. Wu, Y. Yang and Y. Li, *Catalysis Science & Technology*, 2022, **12**, 1610-1618.
10. Y. Mengxia, X. Dan, W. Shuyuan, W. Baoshan, Y. Yong and L. Yongwang, *Fuel*, 2022, **330**, 125671.
11. S. Zhang, L. Chen, Z. Qi, L. Zhuo, J.-L. Chen, C.-W. Pao, J. Su and G. A. Somorjai, *Journal of the American Chemical Society*, 2020, **142**, 16533-16537.
12. D. Xu, B. Wu, P. Ren, S. Wang, C. Huo, B. Zhang, W. Guo, L. Huang, X. Wen, Y. Qin, Y. Yang and Y. Li, *Catalysis Science & Technology*, 2017, **7**, 1342-1350.
13. W. D. Shafer, G. Jacobs, U. M. Graham, V. R. R. Pendyala, M. Martinelli, G. A. Thomas, T. Jermwongratanaachai, A. MacLennan, Y. Hu and B. H. Davis, *Catalysis Letters*, 2018, **148**, 97-107.
14. J. Wang, Q. Liu, K. Li, Y. Yao, J. Yang, X. Ding, S. Chen and X. Wang, *Chemical Engineering Science*, 2025, **301**, 120715.
15. K. Li, Q. Chang, J. Yin, C. Zhao, L. Huang, Z. Tao, Y. Yun, C. Zhang, H. Xiang, Y. Yang and Y. Li, *Journal of Catalysis*, 2018, **361**, 193-203.
16. Q. Zhou, Y. Chen, S. Fan, S. Wang, Z. Qin, M. Dong, J. Wang and W. Fan, *Fuel*, 2023, **337**, 126874.
17. K. Lee and M. Choi, *Journal of Catalysis*, 2016, **340**, 66-75.
18. C. Zhao, B. Wu, Z. Tao, K. Li, T. Li, X. Gao, L. Huang, Y. Yun, Y. Yang and Y. Li, *Catalysis Science & Technology*, 2018, **8**, 2860-2869.
19. S. Ying, Z. Qiuming, Q. Zhangfeng, W. Zhiwei, J. Weiyong, D. Mei, F. Weibin and W. Jianguo, *Microporous and Mesoporous Materials*, 2021, **324**, 111308.
20. S. Wang, Y. Gao, F. Yi, M. Yan, D. Zhu, D. Xu and Y. Li, *Fuel*, 2022, **328**, 125281.
21. J. Wang, P. Zhu, C. Liu, H. Liu, W. Zhang and X. Zhang, *Industrial & Engineering Chemistry Research*, 2022, **61**, 9249-9261.
22. P. Zhang, Y. Yang, Z. Li, B. Liu and C. Hu, *Catalysis Today*, 2020, **353**, 146-152.
23. J. Song, H. Ma, Z. Tian, L. Yan, Z. Xu, Q. Liu and W. Qu, *Applied Catalysis A: General*, 2015, **492**, 31-37.
24. X. Dan, W. Li, J. Yang, B. Zhuoya, S. Angang, L. Guofu, W. Jianmei, D. K. Arthur Ernest, Z. Peng, S. Laizhi, T. Mingxing, L. Tao, T. Zhichao and W. Shuyuan, *Fuel*, 2024, **384**, 134063.